ANNALS OF GEOPHYSICS, 2026; doi:10.4401/ag-9581
OPEN ACCESS

Three-Dimensional Gravity Inversion and Horizontal-Derivative Analysis for Regional Structural and Density-Domain Characterization of the Southern Mountain Zone, East Java, Indonesia

Ajimas Pascaning Setiahadiwibowo[1,2], Sismanto Sismanto[*,1], Salahuddin Husein[3]

(1) Universitas Gadjah Mada, Faculty of Mathematics and Natural Sciences, Department of Physics, Yogyakarta, Indonesia
(2) Universitas Pembangunan Nasional Veteran Yogyakarta, Faculty of Mineral Technology, Geophysical Engineering Department, Yogyakarta, Indonesia
(3) Universitas Gadjah Mada, Faculty of Engineering, Geological Engineering Department, Yogyakarta, Indonesia

Article history: received April 15, 2026; accepted October 16, 2026

Abstract

The Southern Mountain Zone of East Java is a structurally complex volcanic-arc region characterized by strong lateral lithological heterogeneity and limited subsurface constraints. This study uses regional gravity-anomaly analysis, horizontal-derivative methods, and regularized three-dimensional inversion to constrain regional-scale subsurface density variations and identify candidate structural boundaries. Satellite-derived gravity data from the GGMplus dataset were processed to obtain a Complete Bouguer Anomaly ranging from −134.3 to 170.5 mGal and a longer-wavelength Regional Bouguer Anomaly ranging from −130.8 to 132.8 mGal. The regional component is interpreted primarily as a constraint on broad, deeper-seated density variations rather than as a direct or unique image of subsurface geological structures.

Sequential gravity inversion using Singular Value Decomposition (SVD) and Occam regularization was applied to iteratively update the model-base geometry, density distribution, and block thickness. The normalized RMS data misfit decreased from approximately 15.5% to 3.02%, indicating progressively improved agreement between the observed and calculated gravity responses. This reduction represents improved data fitting and should not be interpreted as a direct measure of uncertainty or geological accuracy because gravity inversion remains intrinsically non-unique. The resulting model delineates broad low-, intermediate-, and high-density domains that are consistent with the regional distribution of sedimentary, volcanic, carbonate, and intrusive units.

Horizontal-derivative responses integrated with inversion cross-sections identify several candidate structural boundaries associated with lateral density contrasts. Apparent normal- and reverse-fault styles, including horst-graben- and half-graben-like geometries, are inferred where prominent derivative responses coincide with density-block variations. However, fault dip, displacement, and kinematics are not uniquely resolved from the gravity data. The results therefore provide regional-scale constraints on major subsurface density domains and candidate structural boundaries rather than a unique high-resolution reconstruction of the subsurface.

Keywords: Southern Mountain Zone; Regional basin architecture; Tectonic compartmentalization; Gravity inversion; Horizontal derivative

1. Introduction

The Southern Mountain Zone of East Java represents a structurally complex segment of the southern Java magmatic arc, where Paleogene-Neogene tectono-magmatic activity has produced strong lateral variations in basin geometry, lithology, and structural configuration. Episodic extension, volcanism, sedimentation, and subsequent deformation have generated a compartmentalized subsurface architecture characterized by fault-bounded density domains and locally developed sedimentary depocenters (Smyth, 2005; Prasetyadi et al., 2021a, 2022). The Southern Mountain Zone of East Java has experienced prolonged tectono-magmatic activities since the Paleogene with episodic volcanism, sedimentation and periods of deformation (Smyth, 2005; Hall, 2012; Farisan and Rachman, 2022). Shale- and coal-bearing intervals reported from several formations provide additional stratigraphic evidence that sediment accumulation and preservation occurred within parts of this structurally segmented basin system (Rachman et al., 2016; Rachman and Prasetyadi, 2021). Regional-to-local fault systems are therefore expected to have played an important role in controlling basin segmentation, sediment accommodation, and the spatial distribution of sedimentary and volcanic successions (Prijosoesilo et al., 1993; Clements et al., 2009; Hall et al., 2007).

Gravity measurements and interpretation techniques have long been used to investigate subsurface characteristics when structural detail cannot be imaged with seismic reflection data due to complex surface geology. Gravity measurements provide a complementary dataset that can constrain lateral density variations beneath volcanic cover where seismic data quality is poor, although they do not directly image subsurface structure (Hinze et al., 2012; Vasanthi and Santosh, 2021). This geophysical approach is most appropriately applied at the regional scale because gravity data are sensitive to lateral density variations and can constrain broad basin-related low-density domains, basement-related density highs, and candidate lateral density boundaries. However, these responses should not be interpreted as unique maps of basin geometry, bedrock topography, or fault surfaces (Zhang et al., 2019; Kebede et al., 2020; Vasanthi and Santosh, 2021). Recent studies have shown that global gravity models such as GGMplus can delineate regional anomaly trends and broad density domains after appropriate Bouguer and terrain corrections and spatial filtering (Sİmav and Yildiz, 2021; Safani et al., 2023; Damayanti et al., 2025). Gravity datasets however, suffer from non-uniqueness which can cause ambiguity in interpreting the correct geological model (Mammo, 2012; Oldenburg and Li, 2005; Alvandi et al., 2023; Kafadar, 2019, 2022; Pham, 2024; Soekarno et al., 2025). Derivative techniques, together with regularized inversion and geological constraints, help reduce ambiguity by stabilizing the inverse solution while enhancing regional gradients that may be associated with candidate lateral density boundaries (Constable et al., 1987; Wang et al., 2012; Witter et al., 2016; Ismullah et al., 2018; Saibi et al., 2021; Ombati et al., 2022; Hassan et al., 2024; Tarhan Bal and Karcioglu, 2025).

Indonesia has over one hundred sedimentary basins spread across various tectonic environments, many of which remain poorly understood in terms of subsurface geometry and basin architecture due to patchy data coverage (ESDM, 2022). The South Java Basin is one example, where integrated three-dimensional gravity-based investigations are still limited despite its location on the main island of Java and its geological significance (Hall et al., 2007). This study addresses this gap by applying horizontal derivative analysis and sequential three-dimensional gravity inversion based on Singular Value Decomposition (SVD) and Occam's regularization to regional gravity anomalies obtained from the GGMplus satellite dataset (Constable et al., 1987; Pirttijarvi, 2004; Pirttijärvi, 2014). The main objective is to constrain the regional basin architecture and tectonic compartmentalization of the Southern Mountain Zone by developing a three-dimensional density-domain model and identifying candidate structural boundaries consistent with the observed gravity field and available geological constraints. The resulting framework is used to evaluate the role of fault architecture in basin segmentation, sediment accommodation, and regional tectonic evolution, with petroleum-system significance considered only as a broader geological implication (Hall, 2012; Setiahadiwibowo et al., 2025).

2. Geology of the research area

The Southern Mountains of East Java form part of a long-lived magmatic-arc system whose evolution involved repeated episodes of sedimentation, volcanism, and tectonic deformation (Fig. 1). These processes produced a heterogeneous stratigraphic framework comprising sedimentary, volcaniclastic, carbonate, volcanic, and intrusive units that collectively record the tectono-sedimentary evolution of the region. The stratigraphic succession also records depositional environments related to the development of the back-arc basin system, ranging from shallow-marine

to deeper-marine settings (Farisan and Rachman, 2022). The complexity of this stratigraphy is evidenced by the presence of sedimentary rocks containing organic materials, including shale and coal layers, thus facilitating the accumulation of organic materials (Prasetyadi, et al., 2021b). The tectonic processes in the Southern Mountains are also very important for structurally advantageous hydrocarbon traps (Prijosoesilo et al., 1993). From a regional basin-architecture perspective, these sedimentary intervals can therefore be considered stratigraphic evidence for localized accommodation zones whose distribution may have been influenced by the regional structural framework.

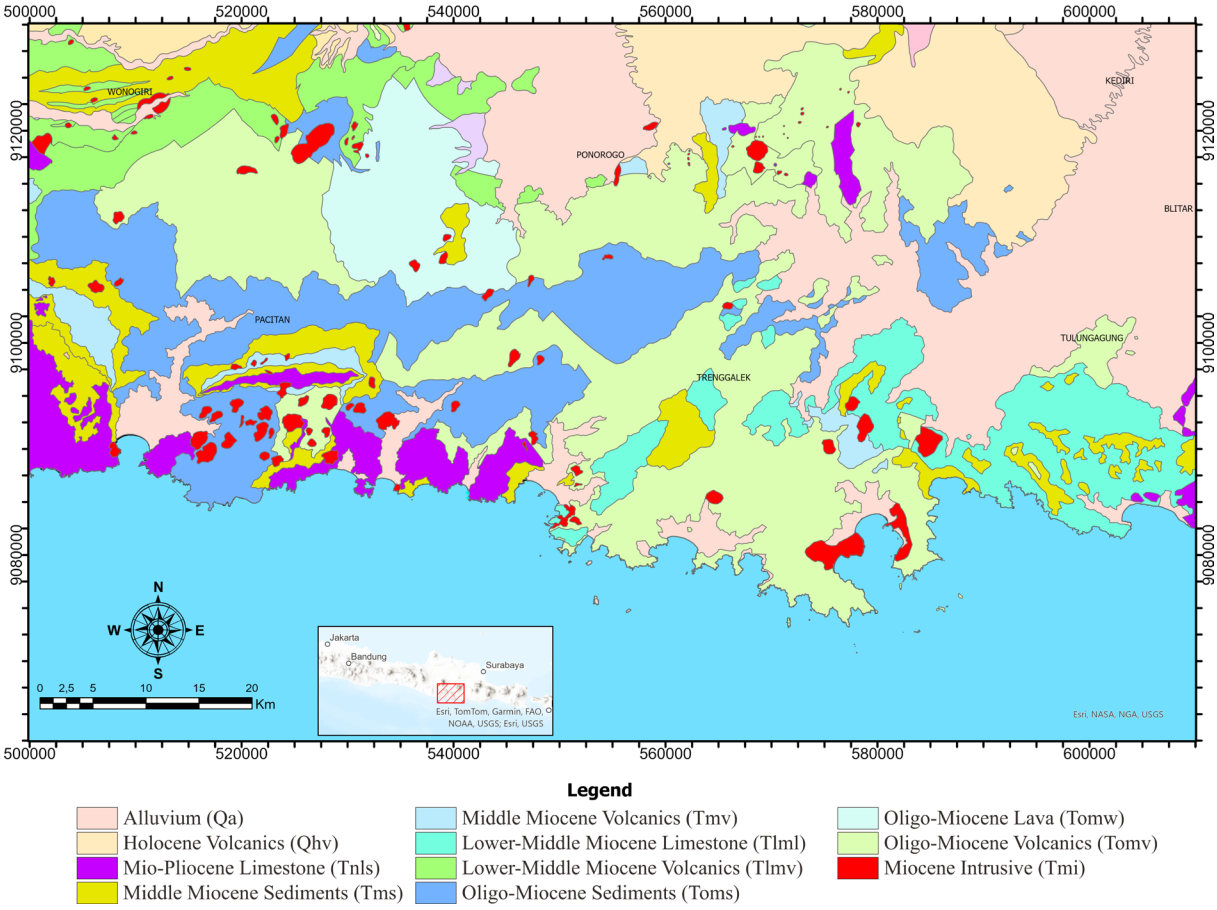


Figure 1. Geological map of the study area showing the principal lithological units used as geological constraints for gravity interpretation (Gafoer and Ratman, 1999).

To establish the geological framework for gravity interpretation, the study area was characterised using published geological maps and previous studies (Gafoer and Ratman, 1999). These sources show that the area comprises diverse lithological units from Quaternary to Oligo-Miocene age, including Alluvium (Qa), Holocene volcanic deposits (Qhv), Mio-Pliocene limestones of the Wonosari Formation (Tnls), Middle Miocene sedimentary units of the Jaten, Nampol, and Oyo formations (Tms), Middle Miocene volcanic rocks of the Wuni Formation (Tmv), Lower-Middle Miocene limestones of the Campurdarat Formation (Tlml), Lower-Middle Miocene volcanics of the Semilir Formation (Tlmv), Oligo-Miocene sedimentary units of the Arjosari and Dayakan formations (Toms), Oligo-Miocene lava flows of the Watupatok Formation (Tomw), Oligo-Miocene volcanic rocks of the Mandalika Formation (Tomv), and Miocene intrusive rocks (Tmi; Fig. 1). Within this stratigraphic framework, shale- and coal-bearing lithologies have been reported from the Middle Miocene Jaten and Nampol formations, parts of the Wuni succession, and the Lower-Middle Miocene Campurdarat unit (Prasetyadi et al., 2022; Rachman et al., 2016; Rachman and Prasetyadi, 2021). In the context of regional basin development, these sediment-bearing successions are significant because their accumulation and preservation indicate the development of localized accommodation space within the evolving basin. Their distribution may therefore provide stratigraphic evidence for fault-controlled depocenters or structurally compartmentalized sub-basins developed between relatively higher-density volcanic, carbonate, and intrusive domains.

Surface exposures of shale- and coal-bearing horizons provide additional geological constraints for evaluating the relationship between sediment distribution and the regional structural framework.

These stratigraphic and lithological variations form the basis for grouping the mapped units into broad density domains for gravity interpretation. Unconsolidated alluvium, young volcanic deposits, and clastic sedimentary successions generally represent relatively low- to moderate-density domains, whereas well-lithified carbonate, older volcanic, and intrusive rocks form comparatively higher-density domains. Therefore, the observed lithological contrasts provide the geological foundation for constructing the initial density model and for interpreting regional gravity gradients and three-dimensional inversion results.

The Southern Mountains in East Java are a structurally complex tectonic zone. The tectonic feature zone has recorded multi-phase deformation throughout the Paleogene to the Quaternary. The geological map at the regional scale shows that the fault trend can be described as dominantly northeast-southwest, west-east, and north-south fault systems (Fig. 2), reflecting the tectonic response to the convergence of the Indo-Australian and Eurasian plates (Pulunggono and Martodjojo, 1994; Prasetyadi et al., 2011; Hall, 2012). Fault-controlled basin segmentation, folds, and the distribution of sedimentary, carbonate, and volcanic rock units are present in the Southern Mountains region. The presence of lithostratigraphic and structural maps also suggests that deformation did not happen in a single tectonic phase, but in multiple phases of extensional, transpressional, and compressional regimes, which have been responsible for fault reactivation and have resulted in complex basin styles (Sribudiyani et al., 2003; Bachri, 2014).

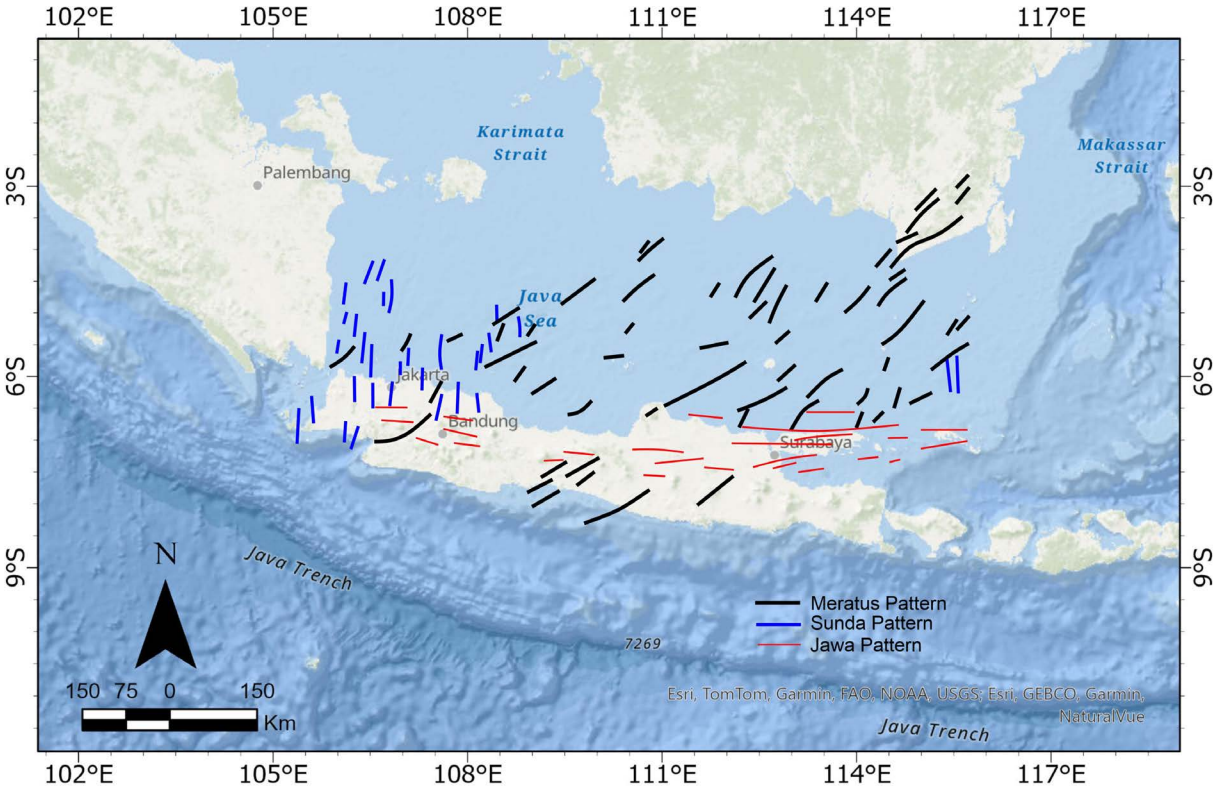


Figure 2. Three directions of fault orientation on Java Island (Pulunggono and Martodjojo, 1994).

3. Data And Methodology

3.1 Data acquisition and processing

Satellite gravity data used in this study were obtained from the Global Gravity Model Plus (GGMplus), developed by Curtin University of Perth in collaboration with the Technical University of Munich. GGMplus is distributed at a nominal grid spacing of approximately 200 m (Hirt et al., 2013); however, this sampling interval should not be interpreted as an equivalent geological resolving capability, particularly for the longer-wavelength gravity components

considered in this study. The gravity data collected represent gravity accelerations, not free-air gravity anomalies; therefore, additional corrections are still needed for the GGMplus satellite gravity data. For instance, within the study area, several corrections must be applied to calculate the Free Air Anomaly (FAA), Simple Bouguer Anomaly (SBA), and Complete Bouguer Anomaly (CBA; Telford et al., 1990). These corrections include subtracting the theoretical normal gravity from the observed gravity values and applying the free-air correction, the simple Bouguer correction, and terrain corrections. Thus, the equation used for the free air correction (δg_{FA}) is written as:

$$\delta g_{FA} = -0.3085672\ \mathrm{h} \tag{1}$$

The topographic height below the measurement location is represented by the value of h, meaning that the free air anomaly (FAA) is

$$\mathrm{FAA} = g_{obs} - g_n - \delta g_{FA} \tag{2}$$

The observed gravitational field is denoted as g_{obs}, while the normal gravitational field on the reference spheroid is represented as g_n. Topographic effects were then corrected by applying the simple Bouguer and terrain corrections separately. The simple Bouguer correction accounts for the gravitational effect of an infinite Bouguer slab. Accordingly, the Simple Bouguer Anomaly (SBA) was calculated from the Free Air Anomaly (FAA) after applying the Bouguer slab correction, following Telford et al., 1990 and Hinze et al., 2012.

$$\mathrm{SBA} = \mathrm{FAA} - (0.04193\rho\beta h) \tag{3}$$

where $\rho\beta$ is the Bouguer reduction density of 2.67 g/cm^3, and h is the elevation in metres. The coefficient 0.04193 represents the unit-converted Bouguer slab factor and should not be interpreted as a terrain correction coefficient. After the simple Bouguer correction is applied, the gravitational effect of surrounding topography is accounted for using a terrain correction derived from the ERTM2160 digital elevation model. This model represents terrain geometry by depicting the relief surrounding each calculation point; consequently, it does not introduce an additional Bouguer slab term. Following the terrain-correction concept of Hammer (1939), the total terrain correction can be expressed as:

$$TC = \sum_{i=1}^{N} \Delta g_i \tag{4}$$

where Δg_i represents the gravitational contribution, expressed in mGal, of the i terrain compartment, and N is the total number of terrain compartments surrounding the calculation point. The total terrain correction (TC), also expressed in mGal, is obtained by summing the gravitational contributions from all terrain compartments. The geometry and relative elevation of each terrain compartment were derived from the ERTM2160 digital elevation model, and the same reduction density of 2.67 g/cm^3 used for the Bouguer correction was applied to the terrain-correction calculation. Consequently, the Complete Bouguer Anomaly (CBA) derived from GGMplus can be computed by summing the Simple Bouguer Anomaly (SBA) and the terrain correction (TC).

$$\mathrm{CBA} = \mathrm{SBA} + TC \tag{5}$$

Regional-residual separation was performed using radially averaged power spectrum (RAPS) analysis, followed by wavenumber-domain band-pass filtering implemented in Oasis montaj to isolate a selected regional-scale wavelength band. The RAPS of the gridded Complete Bouguer Anomaly (CBA) was used to identify the principal change in spectral

slope associated with different characteristic source wavelengths. The regional-residual boundary was defined at approximately 0.05 cycles/km, corresponding to a wavelength of about 20 km. Based on this spectral criterion, a band-pass filter was applied in Oasis montaj with a regional passband of approximately 0.0125-0.05 cycles/km, corresponding to wavelengths of about 80-20 km. Components below 0.0125 cycles/km, corresponding to wavelengths longer than approximately 80 km, were excluded from the selected regional-scale band. A transition band from 0.05 to 0.075 cycles/km, equivalent to wavelengths of about 20-13.3 km, was applied to progressively attenuate the higher-wavenumber components, while components above 0.075 cycles/km were suppressed. The passband, transition, and cut-off limits for the Oasis montaj band-pass filter were specified based on the spectral break identified in the RAPS. These parameters were selected to preserve broad regional-scale density variations while reducing shorter-wavelength contributions associated with shallower sources, topographic effects, and gridding noise. The resulting filtered anomaly is therefore interpreted as a regional-scale constraint on longer-wavelength density variations rather than as a direct or unique image of basement geometry or individual geological structures.

3.2 Horizontal Derivative (Horizontal gradient)

Horizontal derivatives in gravitational anomaly data are defined as variations in the gravitational field between two points separated by a given distance. Horizontal derivative analysis can be conducted using the first horizontal derivative (FHD) or the second horizontal derivative (SHD). Horizontal derivative analysis was applied using the first horizontal derivative (FHD) and second horizontal derivative (SHD) to enhance lateral changes in the gravity field associated with density contrasts and candidate structural boundaries. Here are the equations that are utilized in FHD and SHD computations (Hinze et al., 2012).

$$FHDx = \frac{\partial g}{\partial x} \quad \text{and} \quad FHDy = \frac{\partial g}{\partial y} \tag{6}$$

$$SHDx = \frac{\partial^2 g}{\partial x^2} \quad \text{and} \quad SHDy = \frac{\partial^2 g}{\partial y^2} \tag{7}$$

Figure 3 depicts the gravitational anomalies at extensive vertical interfaces between geological barriers, predicated on varying density anomaly values. Under idealized contact conditions, FHD extrema and SHD zero-crossings may indicate candidate lateral density boundaries; however, these responses do not uniquely define fault geometry (Hinze et al., 2012).

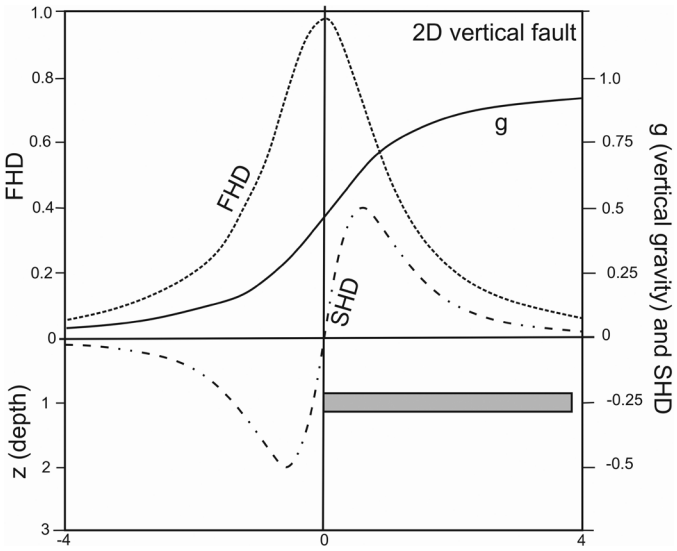


Figure 3. Illustration of gravity anomaly (g), SHD, and FHD (Hinze et al., 2012).

The SHD is used here to highlight candidate lateral density boundaries. Under idealized two-dimensional contact assumptions, the relative amplitudes of the positive and negative SHD lobes may provide a qualitative indication of dip tendency. This relationship is not used to uniquely determine fault dip. The criteria used here to infer the dip of a subsurface structure from the relative magnitudes of the maximum and minimum second-derivative lobes were originally formulated for the second vertical derivative (2VD) (Sumintadireja et al., 2018) (Fig. 4). Their application to the profile-parallel SHD is justified by the fact that, in the source-free region above the causative bodies, the gravity field satisfies Laplace's equation. For a two-dimensional structure with no variation along strike, this gives $\partial^2\Delta g/\partial z^2 = -\partial^2\Delta g/\partial x^2$, so that the second vertical derivative and the profile-parallel second horizontal derivative carry the same information about a density contact and differ only in sign, the maximum and minimum lobes being interchanged between the two operators. Figure 4 presents the criteria expressed in the SHD sign convention adopted throughout this paper. In an idealised vertical or dipping contact model, the FHD reaches an extreme value near the density boundary, whereas the SHD changes sign across the contact, and the relative magnitude of the positive and negative SHD lobes indicates the dip tendency of the contact. Because the amplitude scaling of the two operators is not identical, this relationship is used here only as a qualitative indication of dip direction: SHD interpretation was therefore combined with density-block relationships in the 3D inversion model to support an apparent structural-style interpretation; fault displacement and kinematics are not uniquely resolved.

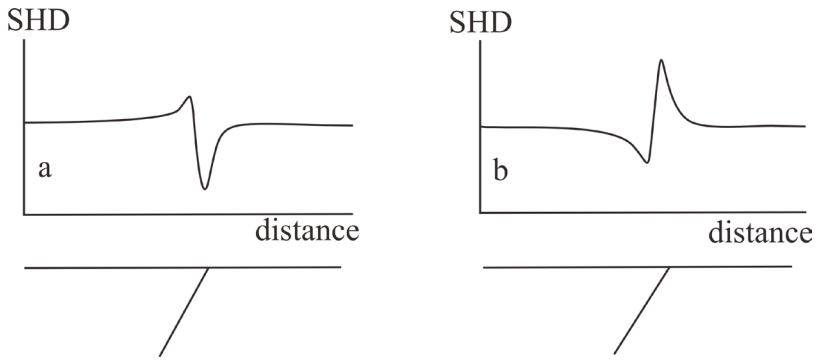


Figure 4. (a) $SHD_{max} < SHD_{min}$ and (b) $SHD_{max} > SHD_{min}$ (Sumintadireja et al., 2018).

3.3 Three-dimensional inversion modelling

Three-dimensional gravity inversion was performed using Bloxer and GRABLOX to construct a density-contrast model consistent with the regional gravity anomaly and geological constraints. Because gravity inversion is inherently non-unique, multiple combinations of density, depth, and geometry may yield similar gravity responses (Blakely, 1995; Oldenburg and Li, 2005). Therefore, regularization and appropriate geological constraints are required to reduce solution ambiguity and obtain a stable and geologically plausible density model (Pirttijärvi, 2014).

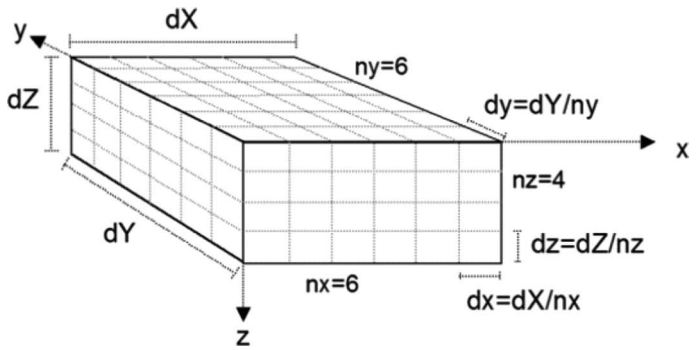


Figure 5. The initial block model of size dX dY dZ is divided into minor blocks nx ny nz of size dx dy dz in Grablox and Bloxer (Pirttijärvi, 2014).

A rectangular prism used for inversion, in which the subsurface volume is divided into a three-dimensional array of smaller blocks, is shown in Fig. 5. Each block is assigned spatial dimensions and a density contrast, allowing the model parameters to be updated iteratively during inversion. The inversion was constrained by the geometry of the initial block model and the regional geological framework. The model domain extends to a depth of 8 km and consists of eight layers in the vertical direction, with 50 × 25 blocks in the horizontal directions. A background density of 2.38 g/cm^3, representative of the dominant lithologies in the study area, was adopted as the reference density, and the inversion solved for density contrasts relative to this value. Physical parameters such as block coordinates (x, y, z) and density values are entered to generate the first model. The inversion procedure was formulated iteratively by first defining the data residual as:

$$e = d_{obs} - d_{cal} \tag{8}$$

where d_{obs} represents the observed gravity data, d_{cal} is the gravity response calculated from the current model, and e represents the discrepancy between them (Menke, 2018). At each iteration, the relationship between the data residual and the required change in model parameters is linearised as:

$$e = J\Delta m \tag{9}$$

where J is the Jacobian or sensitivity matrix and Δm represents the correction applied to the model parameters. In the Singular Value Decomposition (SVD) approach, the Jacobian matrix is decomposed as

$$J = U\Sigma V^T \tag{10}$$

where U and V contain the left and right singular vectors, respectively, and Σ contains the singular values. The model correction can subsequently be estimated from:

$$\Delta m = V\Sigma^{-1}U^T e \tag{11}$$

allowing the model parameters to be progressively updated toward a better fit between the observed and calculated gravity responses (Aster et al., 2018).

Because gravity inversion is inherently non-unique and small singular values may lead to unstable model updates, damping and regularisation are required to stabilise the inverse solution (Menke, 2018; Pirttijärvi, 2014). In the Occam approach, regularisation is introduced by seeking a smooth model that provides an acceptable fit to the observed data (Constable et al., 1987). Conceptually, the objective function may be expressed as:

$$\Phi(m) = \|d_{obs} - d_{cal}\|^2 + \lambda\|Lm\|^2 \tag{12}$$

where the first term represents the data misfit, the second term represents model roughness, L is the smoothing operator, and λ controls the trade-off between fitting the observed data and maintaining model smoothness (Constable et al., 1987; Aster et al., 2018). In GRABLOX, the Occam-type regularization suppresses unnecessary variations between adjacent model blocks while progressively improving the fit to the observed gravity field. The regularization therefore balances model smoothness against data misfit, while convergence was assessed from the progressive reduction and stabilization of the normalized RMS data misfit between successive inversion stages.

The goodness of fit between the observed gravity data and the calculated model response was evaluated using the normalized root-mean-square (RMS) data misfit implemented in GRABLOX (Pirttijärvi, 2014):

$$RMS(\%) = 100\sqrt{\frac{1}{M}\sum_{i=1}^{M}\left(\frac{d_i - y_i}{\Delta d}\right)^2} \tag{13}$$

where d_i is the observed gravity anomaly at the i data point, y_i is the corresponding gravity response calculated from the current model, M is the total number of gravity observations, and $\Delta d = d_{max} - d_{min}$ is the range of the observed gravity data used for normalization. Accordingly, the RMS value reported in this study represents a normalized data misfit rather than an estimate of uncertainty in density, depth, or subsurface geometry. A decreasing RMS therefore indicates progressively better agreement between the observed and calculated gravity responses but does not imply uniqueness of the recovered geological model.

4. Results

4.1 Complete Bouguer Anomaly (CBA)

The Complete Bouguer Anomaly (CBA) map (Fig. 6) shows gravity anomaly values ranging from −134.3 to 170.5 mGal. Low anomalies, represented mainly by blue to cyan colours, occur predominantly in the eastern, northeastern, and northern parts of the study area and range from approximately −134.3 to −4.6 mGal. Intermediate anomalies, represented by green to yellow-orange colours, range approximately from −4.6 to 43.2 mGal. Higher anomalies, represented mainly by red to purple colours, range approximately from 43.2 to 170.5 mGal. These anomaly variations reflect the superimposed effects of density contrasts across different spatial scales; therefore, the CBA was subsequently subjected to regional-residual separation prior to further interpretation.

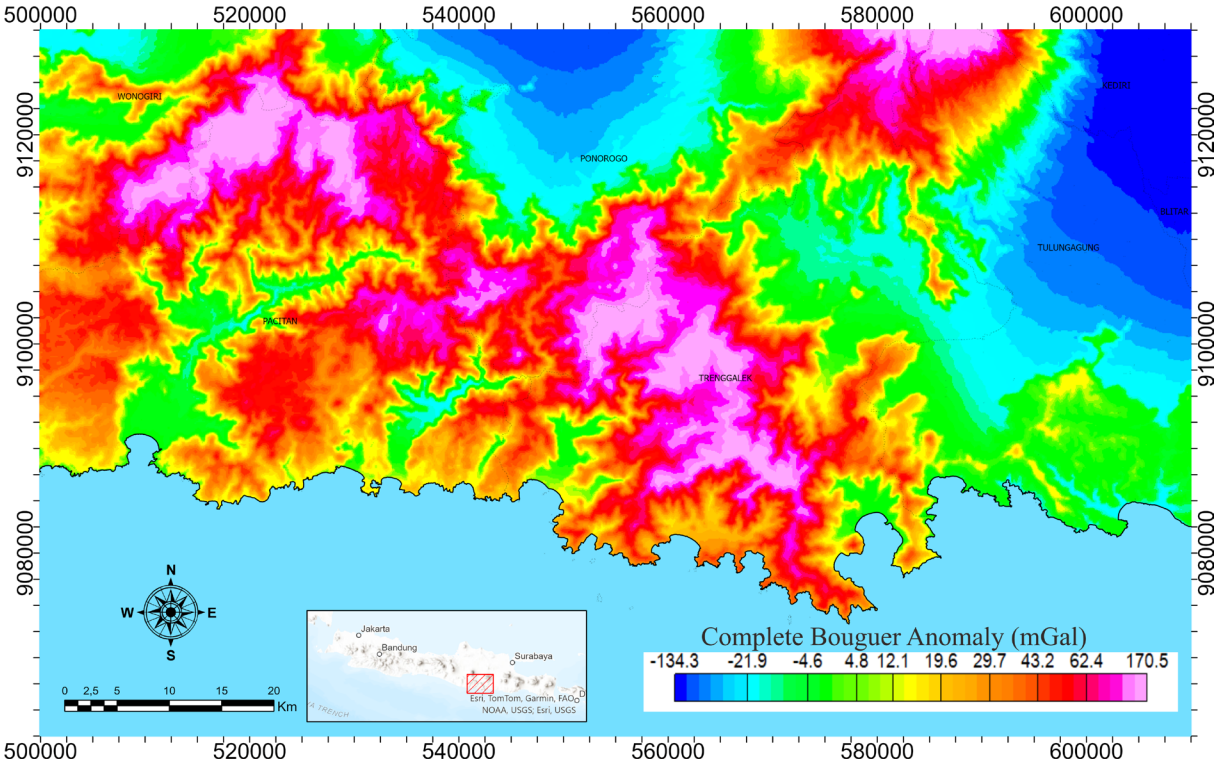


Figure 6. Complete Bouguer Anomaly (CBA) map in the study area.

4.2 Regional anomaly map

Consistent with this filtering result, the regional anomaly map generally resembles the Complete Bouguer Anomaly (CBA) map, but it displays a smoother pattern because the shorter-wavelength components have been attenuated. This smoother distribution is interpreted as more sensitive to longer-wavelength, deeper-seated density variations than to shallow or local anomaly sources (Soekarno et al., 2025). As shown in Fig. 7, the regional gravity anomaly ranges from −130.8 to 132.8 mGal. Lower regional anomalies, represented mainly by blue to cyan colours, occur predominantly in the northeastern, eastern, and northern parts of the study area and range approximately from −130.8 to −3.1 mGal. Intermediate anomalies, represented by green to yellow-orange colours, range approximately from −3.1 to 42.4 mGal, whereas higher anomalies, represented mainly by red to purple colours, range from approximately 42.4 to 132.8 mGal. The lower-anomaly domains may be associated with relatively lower-density subsurface materials, including possible sedimentary accumulations, whereas higher anomalies indicate comparatively higher-density domains. These interpretations remain regional-scale constraints rather than unique lithological determinations. Overall, the study area is dominated by high anomaly values, consistent with its position within the Southern Mountain Zone, where siliciclastic, volcanoclastic, volcanic, and carbonate rock formations are widely exposed (Smyth, 2005). Thus, the regional anomaly map provides a regional-scale constraint on the density framework associated with the major lithological domains in the study area.

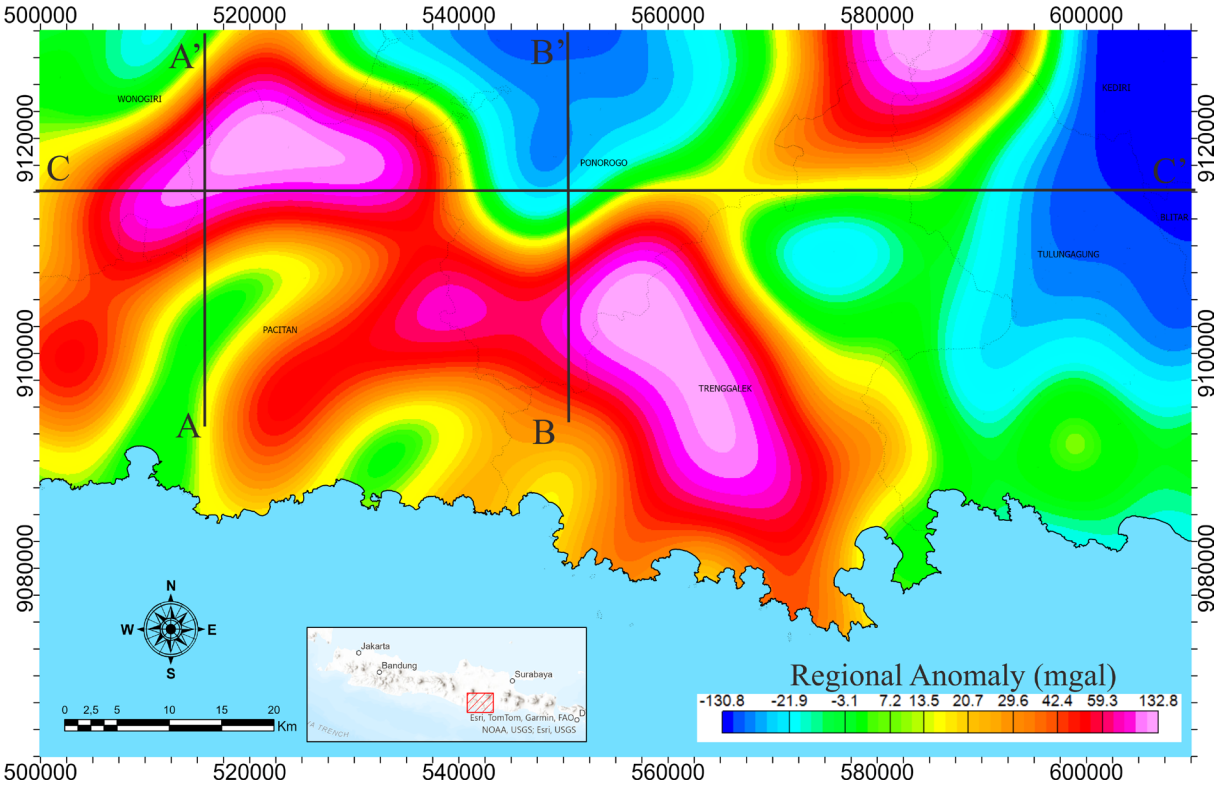


Figure 7. Regional anomaly map of the study area derived from the CBA. Persistent high regional anomalies in purple are interpreted as broad relatively higher-density domains.

4.3 Inversion modelling

The computed and differential results for the base, density, and height parameters were obtained from the inversion procedure using Singular Value Decomposition (SVD) and Occam inversion (Fig. 8). These methods are used to obtain a regularized density model that provides an acceptable fit to the observed gravity data while limiting instability associated with the non-uniqueness of the inverse problem. Sequential SVD-Occam inversion progressively improved the agreement between the observed and calculated gravity responses (Fig. 8). The inversion was conducted

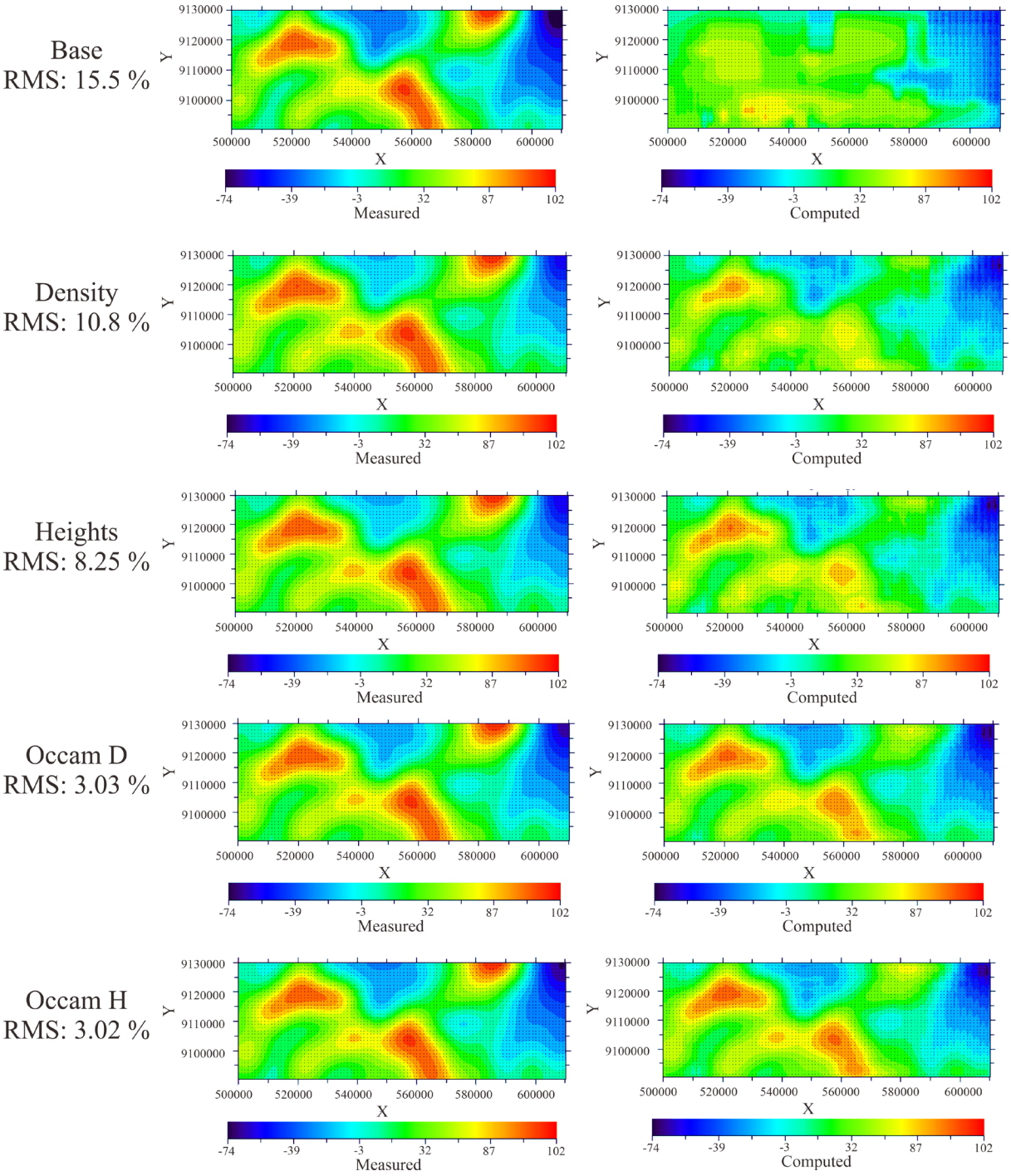


Figure 8. Comparison between observed and calculated gravity responses during sequential GRABLOX inversion stages. The normalized RMS data misfit decreases from 15.5% during base optimisation to 10.8% after density inversion, 8.25% after height refinement, 3.03% after Occam density optimisation, and 3.02% after Occam height optimisation.

through successive optimization of the model base, density, and block height, followed by Occam density and height regularization. The normalized RMS data misfit was used to quantitatively evaluate the improvement achieved at each inversion stage (Oldenburg and Li, 2005). The normalized RMS data misfit was used only to quantify the agreement between the observed and calculated gravity responses at each inversion stage. It therefore provides a measure of data fit and should not be interpreted as an uncertainty estimate for model density, depth, geometry, or geological accuracy (Constable et al., 1987; Oruc and Balkan, 2023).

The first iteration step concentrates on modelling the base of the subsurface model. This represents the base geometry or depth limit of each layer. The resulting anomaly contour is still far from the anomaly measured (normalized RMS

data misfit of 15.5%). The relatively high initial RMS indicates that the calculated gravity response differs substantially from the observed gravity field at this stage, so additional model parameters were subsequently updated.

The second step involves a density inversion that controls the gravity response. The normalized RMS data misfit decreased further to 10.8% in this step, yielding a better fit between the calculated and measured values. The first results of the inversion matched when the calculated and measured contours overlapped. Density inversion helps constrain lateral and vertical density variations that may be related to lithological changes.

In the third step, the block heights are adjusted by changing the thickness of the subsurface units. The normalized RMS data misfit decreased further to 8.25%. As shown in the figure above, the modelled gravity response is approaching the field data. The calculated anomaly now envelops the measured anomaly. This indicates that the model response is increasingly consistent with the observed gravity data. Adjusting block thickness changes the volume of anomalous mass represented by each block, thereby improving the fit to the observed anomaly.

The normalized RMS data misfit progressively decreased from approximately 15.5% during the initial base optimisation to 10.8% following density inversion and 8.25% after height refinement. Subsequent Occam regularization further reduced the normalized RMS misfit to 3.03% for density optimisation (Occam D) and 3.02% for height optimisation (Occam H). This progressive reduction demonstrates improved agreement between the observed gravity anomalies and the responses calculated from the inversion model. However, the final RMS value should not be interpreted as a direct measure of geological accuracy or model uncertainty because gravity inversion remains intrinsically non-unique.

4.4 3D Model

Subsurface modelling was conducted using the filtered regional anomaly, which is interpreted as being more sensitive to broad, longer-wavelength density variations than to shallow or local anomaly sources. Horizontal geological maps were also incorporated as references to aid in creating the starting block model. An initial model was constructed for the study area with a total vertical extent of 8 km, discretized into eight layers. The model was further discretized into 50 × 25 blocks along the x- and y-directions. The inversion-derived density contrasts were converted to absolute density values for interpretation by adding the adopted background density. This study adopted 2.38 g/cm^3, the average rock density within the study area, as the background density for this study (Wijayanti et al., 2009; Ismullah et al., 2018; Nurhandoko et al., 2019; Sutasoma et al., 2022; Setiahadiwibowo et al., 2025). This background was established from the prevailing lithology in the area.

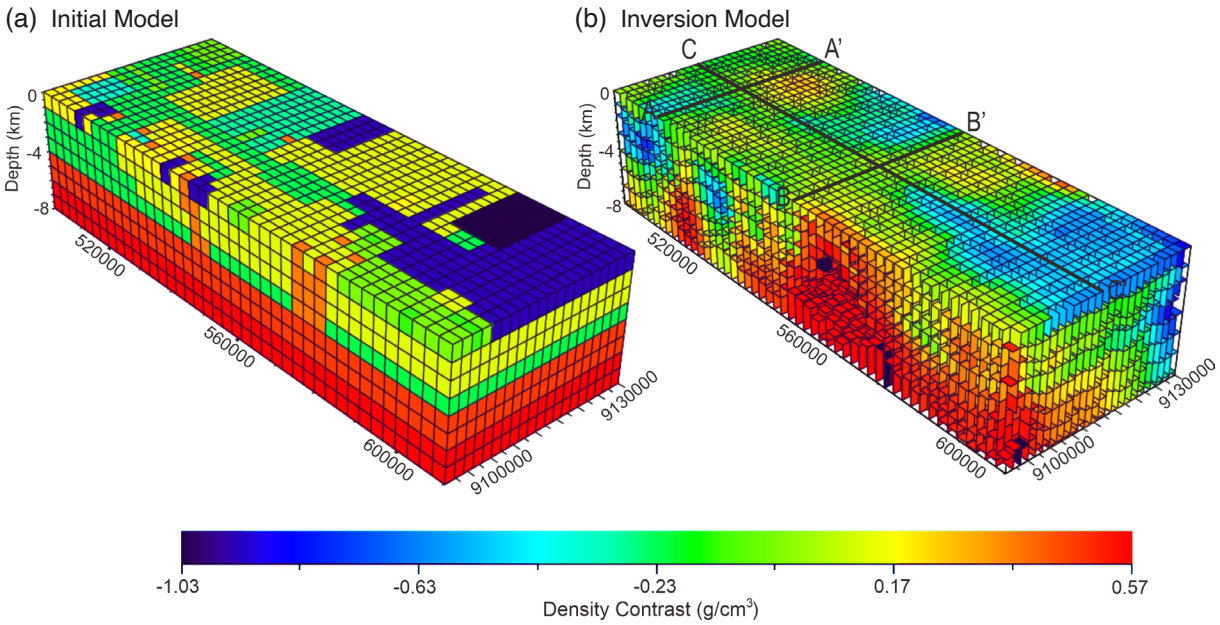


Figure 9. (a) The initial 3D conceptual model and (b) the refined final model produced through 3D inversion modelling.

Figure 9 presents the initial and inverted models as three-dimensional block models of density contrast, with a color scale ranging from –1.03 to 0.57 g/cm^3. This format enables visual comparison of subsurface density changes before and after inversion. The absolute density of each block was calculated by adding the corresponding density-contrast value to the adopted background density. The initial model (Fig. 9a) shows the starting density-contrast distribution derived from the regional geological framework and model parameterization. Its discrete, blocky pattern reflects the initial parameterization before gravity-inversion optimization.

The inversion model (Fig. 9b) represents the final density-contrast distribution obtained after iterative inversion of the regional gravity anomaly. During the inversion, the model parameters were progressively adjusted to improve the agreement between the observed and calculated gravity responses while maintaining model smoothness through regularization. Compared with the initial model, the final model exhibits a smoother, more continuous distribution of density contrasts, delineating broad subsurface density domains and lateral density variations. These variations can be interpreted in relation to the regional geological framework and may reflect differences in lithology and major structural boundaries.

The range of density-contrast values derived from the inversion provides a basis for geologically constrained correlation with broad lithological domains within the study area. Because gravity inversion is inherently non-unique and different lithologies may exhibit overlapping density ranges, the following lithological assignments should be regarded as interpretations consistent with the regional geological framework rather than unique determinations. The lowest density-contrast interval, from –1.07 to –0.69 g/cm^3, corresponding to absolute density values of 1.31-1.69 g/cm^3, is interpreted as being consistent with relatively low-density unconsolidated alluvial deposits (Fig. 10a), which generally consist of loose sediments with high porosity and low bulk density (Manger, 1963). Slightly higher contrast density values, ranging from –0.68 g/cm^3 to –0.57 g/cm^3 or density values 1.7 g/cm^3 to 1.81 g/cm^3, are associated with Holocene Volcanics (Fig. 10b), which typically include young, less compacted volcanic materials such as pyroclastic flows or lava flows near the surface.

In the lower middle Miocene sequence, the Semilir Formation, representing Lower-Middle Miocene Volcanics (Fig. 10c), show contrast density value between –0.56 g/cm^3 to –0.38 g/cm^3 or density value 1.82 g/cm^3 to 2 g/cm^3. These density values are consistent with moderately compacted volcanic rocks that may exhibit variable degrees of alteration. Adjacent to these volcanic units, the Oligo-Miocene sedimentary units (Fig. 10d), which include the Arjosari and Dayakan formations, display contrast density values from –0.37 g/cm^3 to –0.18 g/cm^3 or absolute density values from 2.01 g/cm^3 to 2.20 g/cm^3, suggesting the presence of interbedded clastic sediments such as sandstone, siltstone, or shale, which typically exhibit lower densities due to higher porosity.

The density-contrast interval from –0.17 g/cm^3 to –0.03 g/cm^3, corresponding to absolute densities or 2.21 g/cm^3 to 2.35 g/cm^3, is interpreted as consistent with the Oligo-Miocene lava-flow domain of the Watupatok Formation (Fig. 10e), based on its spatial relationship with the mapped geology and the relatively higher density expected for compact volcanic rocks. The Middle Miocene volcanic domain correlated with the Wuni Formation (Fig. 10f) exhibits density-contrast values of approximately –0.02 to 0.02 g/cm^3, corresponding to absolute densities of 2.36-2.40 g/cm^3. These values are compatible with volcanic rocks whose bulk density may vary with alteration and weathering. The Middle Miocene sedimentary domain comprising the Jaten, Nampol, and Oyo formations (Fig. 10g) is correlated with density-contrast values of approximately 0.03-0.08 g/cm^3, corresponding to absolute densities of 2.41-2.46 g/cm^3, consistent with relatively compact sedimentary successions with moderate lithification.

The higher contrast density intervals indicate more consolidated carbonate and igneous units. The Mio-Pliocene limestone (Fig. 10h) of the Wonosari Formation shows density-contrast values of 0.09-0.12 g/cm^3, corresponding to 2.47-2.50 g/cm^3, while the Lower-Middle Miocene limestone (Fig. 10i) of the Campurdarat Formation has density-contrast values of 0.13-0.22 g/cm^3, corresponding to 2.51-2.60 g/cm^3; both intervals reflect well-lithified carbonate deposits. Furthermore, the Oligo-Miocene Volcanics (Fig. 10j) of the Mandalika Formation exhibit a density range from 0.23 g/cm^3 to 0.37 g/cm^3, corresponding to density values of 2.61 g/cm^3 to 2.75 g/cm^3, indicating dense volcanic rocks with limited porosity. The highest values, ranging from 0.38 g/cm^3 to 0.57 g/cm^3, or from 2.76 g/cm^3 to 2.95 g/cm^3, correspond to the Miocene Intrusive Rocks (Fig. 10k), which are typically crystalline and dense, and represent the deepest, most compact lithologies within the study area. While the density-contrast model characterizes the broad subsurface density domains, structural boundaries were further evaluated using horizontal-derivative analysis along selected cross-sections.

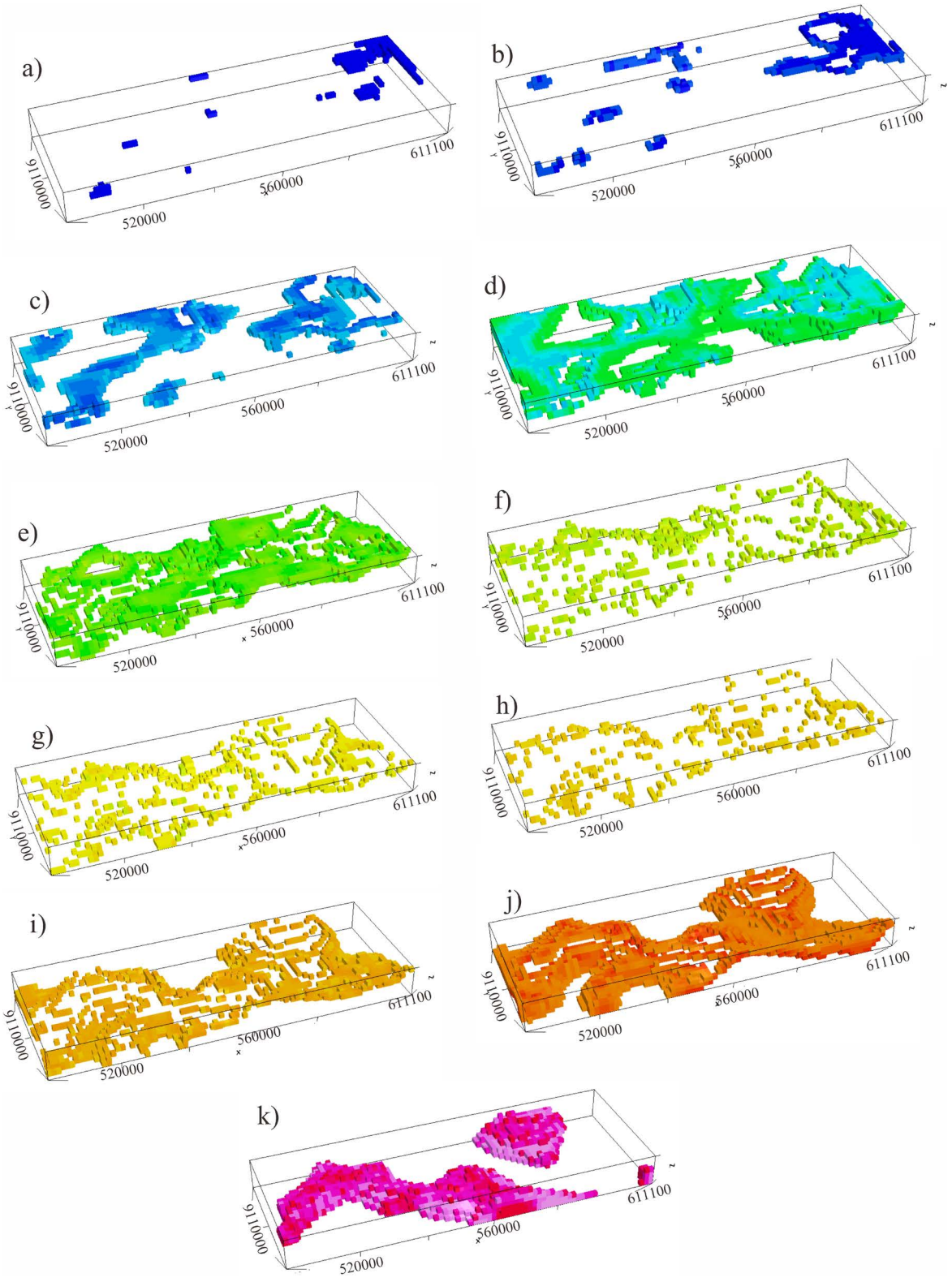


Figure 10. Spatial distribution of density-contrast intervals derived from the 3D gravity inversion: (a) Alluvium, −1.07 to −0.69 g/cm^3; (b) Holocene volcanics, −0.68 to −0.57 g/cm^3; (c) Lower-Middle Miocene volcanics (Semilir Formation), −0.56 to −0.38 g/cm^3; (d) Oligo-Miocene sedimentary units (Arjosari and Dayakan formations), −0.37 to −0.18 g/cm^3; (e) Oligo-Miocene lava flows (Watupatok Formation), −0.17 to −0.03 g/cm^3; (f) Middle Miocene volcanics (Wuni Formation), −0.02 to 0.02 g/cm^3; (g) Middle Miocene sediments (Jaten, Nampol, and Oyo formations), 0.03-0.08 g/cm^3; (h) Mio-Pliocene limestone (Wonosari Formation), 0.09-0.12 g/cm^3; (i) Lower-Middle Miocene limestone (Campurdarat Formation), 0.13-0.22 g/cm^3; (j) Oligo-Miocene volcanics (Mandalika Formation), 0.23-0.37 g/cm^3; and (k) Miocene intrusive rocks, 0.38-0.57 g/cm^3.

4.5 Derivative analysis

Candidate structural boundaries within the study area were evaluated using three cross-sectional profiles. The regional gravity anomaly (red dashed line), first horizontal derivative (FHD; blue line), and second horizontal derivative (SHD; orange line) are plotted along the selected profiles in Figs. 11a-13a, while the corresponding three-dimensional inversion cross-sections are shown in Figs. 11b-13b. These derivative curves enhance changes in the gravity field associated with lateral density discontinuities and potential structural boundaries. Critical points, particularly prominent gradient changes and SHD extrema or zero-crossing relationships, are used together with density changes in the inversion sections to identify candidate structural boundaries.

The 3D inversion model cross-section shows three-dimensional data, which the Grablox software uses to create graphs that match regional anomaly profiles at their original coordinates. The black lines superimposed on the inversion sections indicate candidate fault boundaries inferred from the derivative responses. Their interpretation is strengthened where prominent derivative gradients coincide spatially with abrupt changes in density contrast within the inversion model.

The qualitative dip tendency of each candidate boundary was inferred following the lobe-amplitude criterion of Sumintadireja et al. (2018), adapted to the SHD as described in Section 3.2. An apparent normal or reverse sense of offset was then assigned from the relative vertical position of higher-density blocks on either side of each boundary in the inversion section. This classification is an interpretation of the density-block geometry, not a direct determination of fault dip, displacement, or kinematics. The A-A′, B-B′, and C-C′ profiles were selected to intersect the most pronounced regional gravity gradients and structural boundaries identified by the horizontal derivative analysis. Profiles A-A′ and B-B′ are oriented approximately south-north to evaluate lateral density and structural variations across contrasting gravity domains, whereas C-C′ is oriented west-east to provide an approximately orthogonal view of the subsurface architecture. The profiles also cross zones characterized by prominent FHD responses, SHD variations, and contrasting density distributions in the inversion model. Consequently, these three sections provide representative views of the main candidate fault-controlled boundaries, basin geometry, and lithological contrasts within the study area.

4.5.1 Cross-section south to north (A-A′)

Cross-section A-A′ is oriented approximately south-north. In Fig. 11a, three candidate fault boundaries are identified from the combined responses of the regional gravity anomaly, FHD, and SHD profiles. Their qualitative dip tendencies are evaluated from the relative SHD lobe amplitudes and are summarized in Table 1. Features 1 and 2 show southward dip tendencies, whereas feature 3 shows a northward dip tendency. The candidate boundaries identified in Fig. 11a are then projected onto the three-dimensional inversion density cross-section in Fig. 11b to evaluate their relationship with lateral density contrasts and density-block geometry. Based on these relationships, features 2 and 3 are interpreted as apparent normal-fault styles, whereas feature 1 is interpreted as an apparent reverse-fault style. The apparent normal-fault geometries are characterized by relative downward offsets of higher-density blocks adjacent to lower-density domains, whereas the apparent reverse-fault geometry is associated with a relative upward offset of a higher-density block. Feature 1 shows a comparatively weak FHD response in Fig. 11a and is therefore regarded as a lower-confidence interpretation. These apparent structural interpretations are based on the combined derivative and density-contrast patterns and should not be regarded as unique determinations of fault dip, displacement, or kinematics.

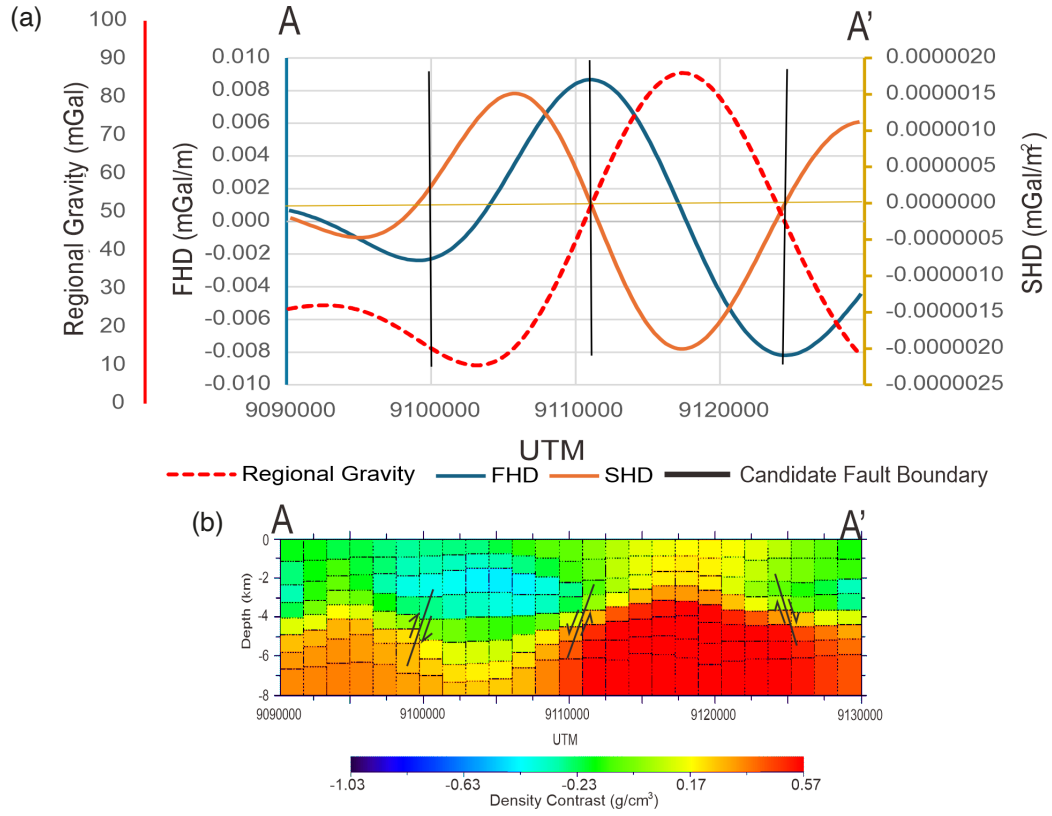


Figure 11. Cross-section A-A′ showing (a) regional gravity, FHD, and SHD profiles with candidate fault-boundary positions and qualitative dip tendencies, and (b) the corresponding three-dimensional inversion density cross-section showing lateral density contrasts and apparent fault styles.

Table 1. Results of derivative analysis of cross section A-A′.

No	|SHD min| (mGal/m²)	|SHD max| (mGal/m²)	Qualitative dip tendency	Apparent structural interpretation
1	0.000000475	0.000001507	SHD min (South)	Apparent Reverse Fault
2	0.000002005	0.000001507	SHD max (South)	Apparent Normal Fault
3	0.000002005	0.000001089	SHD max (North)	Apparent Normal Fault

4.5.2 Cross section south to north (B-B′)

Cross-section B-B′ is oriented approximately south-north. In Fig. 12a, three candidate fault boundaries are identified from the combined regional gravity, FHD, and SHD responses. Their qualitative dip tendencies are summarized in Table 2. Features 1 and 2 show southward dip tendencies, whereas feature 3 shows a northward dip tendency. The candidate boundaries identified from the derivative responses in Fig. 12a are subsequently projected onto the three-dimensional inversion density cross-section in Fig. 12b to evaluate their association with lateral density contrasts and density-block geometry. Based on these relationships, feature 1 is interpreted as an apparent normal-fault style, whereas features 2 and 3 are interpreted as apparent reverse-fault styles. The apparent normal-fault geometry is associated with a relative downward offset of a higher-density block, whereas the apparent reverse-fault geometries are associated with relative upward offsets of higher-density blocks adjacent to lower-density domains. Feature 3 is characterized by a comparatively weak FHD response in Fig. 12a and is therefore regarded as

a lower-confidence interpretation. The apparent fault styles represent interpretations of the combined derivative and density-block patterns and do not uniquely determine fault dip, displacement, or kinematics.

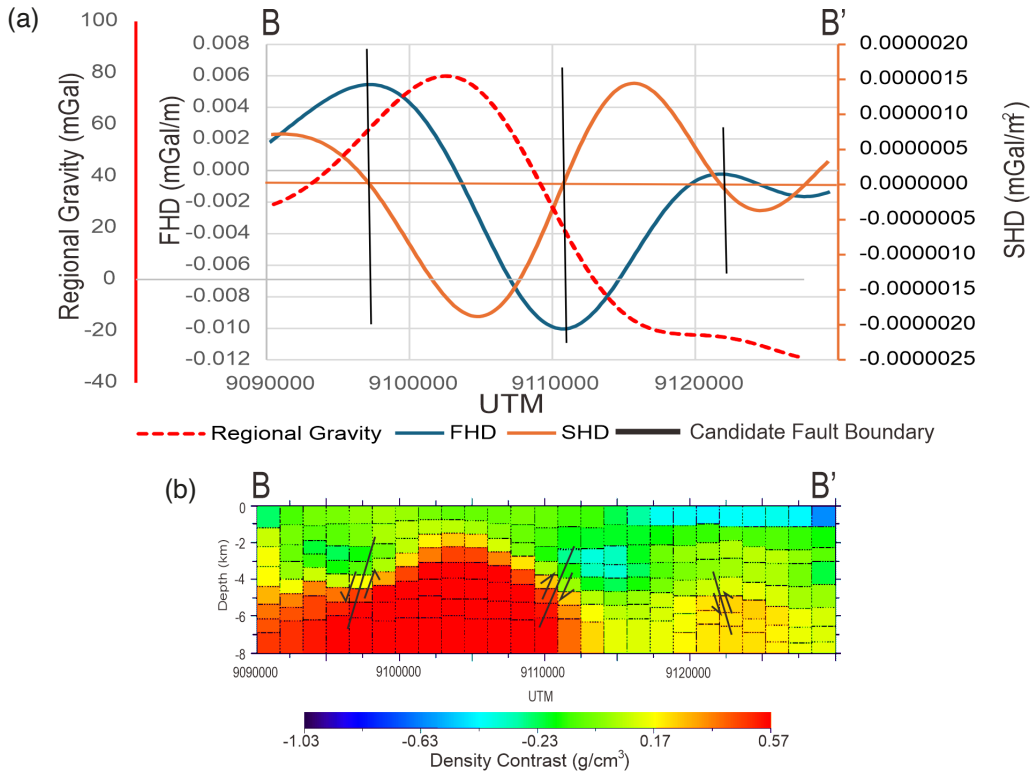


Figure 12. Cross-section B-B′ showing (a) regional gravity, FHD, and SHD profiles with candidate fault-boundary positions and qualitative dip tendencies, and (b) the corresponding three-dimensional inversion density cross-section showing lateral density contrasts and apparent fault styles.

Table 2. Results of derivative analysis of cross section B-B′.

No	|SHD min| (mGal/m²)	|SHD max| (mGal/m²)	Qualitative dip tendency	Apparent structural interpretation
1	0.000001882	0.000000720	SHD max (South)	Apparent Normal Fault
2	0.000001882	0.000001443	SHD max (South)	Apparent Reverse Fault
3	0.000000371	0.000001443	SHD min (North)	Apparent Reverse Fault

4.5.3 Cross-section west to east (C-C′)

Cross-section C-C′ is oriented west-east. In Fig. 13a, nine candidate fault boundaries are identified from the combined regional gravity, FHD, and SHD responses. The qualitative dip tendencies summarized in Table 3 comprise five westward- and four eastward-dipping features. These candidate boundaries are then projected onto the corresponding three-dimensional inversion density cross-section in Fig. 13b to evaluate their relationships with lateral density contrasts and density-block geometry. Based on these relationships, seven boundaries are interpreted as apparent normal-fault styles and two as apparent reverse-fault styles. The apparent normal-fault geometries are associated with relative downward offsets of higher-density blocks, whereas the apparent reverse-fault geometries

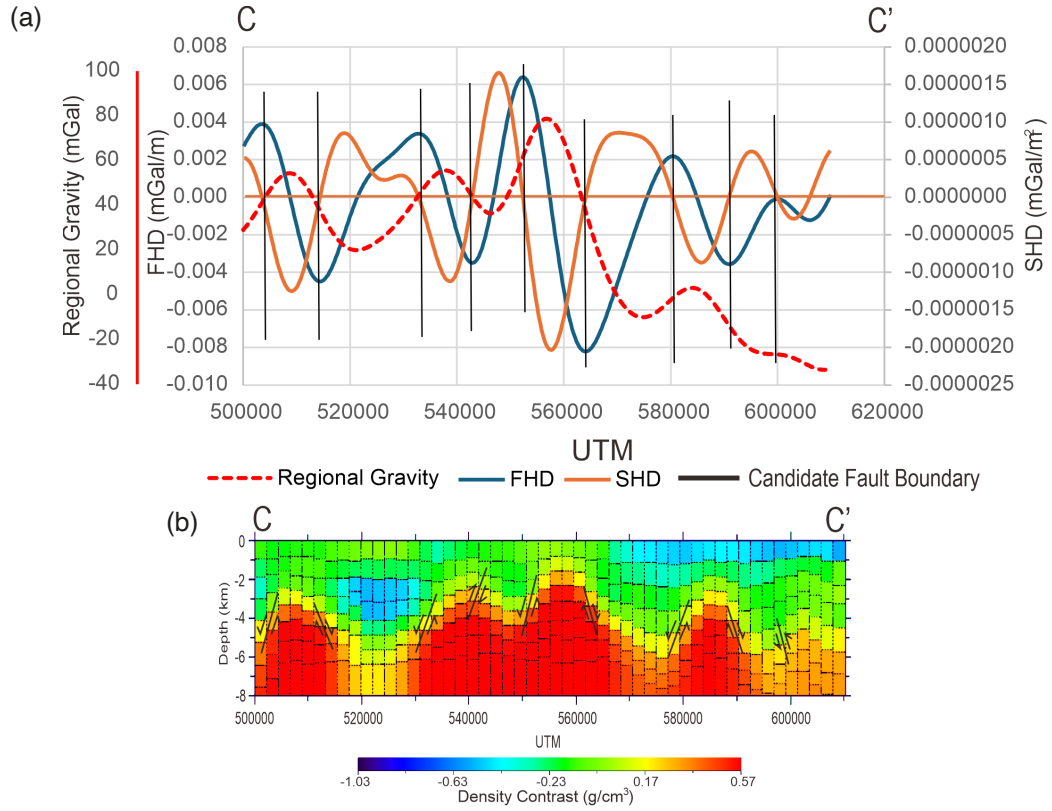


Figure 13. Cross-section C-C′ showing (a) regional gravity, FHD, and SHD profiles with candidate fault-boundary positions and qualitative dip tendencies, and (b) the corresponding three-dimensional inversion density cross-section showing lateral density contrasts and apparent fault styles.

Table 3. Results of derivative analysis of cross-section C-C′.

No	|SHD min| (mGal/m^2)	|SHD max| (mGal/m^2)	Qualitative dip tendency	Apparent structural interpretation
1	0.000001251	0.000000521	SHD max (West)	Apparent Normal Fault
2	0.000001251	0.000000853	SHD max (East)	Apparent Normal Fault
3	0.000001120	0.000000287	SHD max (West)	Apparent Normal Fault
4	0.000001120	0.000001655	SHD min (West)	Apparent Reverse Fault
5	0.000002035	0.000001655	SHD max (West)	Apparent Normal Fault
6	0.000002035	0.000000858	SHD max (East)	Apparent Normal Fault
7	0.000000871	0.000000858	SHD max (West)	Apparent Normal Fault
8	0.000000871	0.000000610	SHD max (East)	Apparent Normal Fault
9	0.000000287	0.000000610	SHD min (East)	Apparent Reverse Fault

are associated with relative upward offsets of higher-density basement or volcanic blocks against lower-density domains. The resulting density-block arrangement is compatible with horst-graben- to half-graben-like geometries. Features 7-9, located in the eastern part of the profile, show relatively weak FHD responses and/or low SHD amplitudes in Fig. 13a and are therefore regarded as lower-confidence interpretations. These apparent structural styles reflect the combined derivative and density-contrast patterns and should not be interpreted as unique determinations of fault displacement or kinematics.

5. Discussion

The regional gravity pattern of the Southern Mountain Zone reveals a heterogeneous upper-crustal architecture dominated by relatively high-density volcanic, carbonate, and intrusive domains separated locally by lower-density zones. Rather than representing isolated lithological variations, this arrangement is interpreted as a regional density-domain framework reflecting the tectono-magmatic evolution of the southern Java arc. Local gravity lows may represent areas of comparatively greater sediment accumulation and therefore constitute candidate depocenters within a structurally compartmentalized intra-arc/back-arc basin system. Their spatial relationship with major lateral density boundaries suggests that regional fault architecture may have controlled the distribution of accommodation space and the segmentation of the basin into discrete structural compartments. Within this regional framework, the occurrence of shale- and coal-bearing intervals in the Jaten, Nampol, Wuni, and Campurdarat successions provides independent stratigraphic evidence that sediment accommodation and preservation occurred locally within the evolving basin. These intervals should not be interpreted from gravity data alone; rather, their documented occurrence supports the geological plausibility of sediment-filled compartments or depocenters associated with the broader fault-controlled basin architecture. These interpretations should nevertheless be regarded as regional-scale constraints rather than unique determinations of basin geometry or lithology. Gravity data primarily constrain variations in subsurface density and the locations of major lateral density boundaries, and lithologies with overlapping density ranges cannot be uniquely distinguished. Consequently, the lithological and structural assignments presented in the inversion model represent geologically constrained interpretations rather than unique solutions.

The progressive reduction in normalized RMS data misfit from 15.5% to 3.02% indicates improved agreement between the observed gravity anomaly and the response calculated from the inversion model. This reduction indicates convergence toward a model that reproduces the measured gravity field more closely; however, it does not demonstrate that the recovered density distribution, depths, or geometries are uniquely correct. Gravity inversion remains intrinsically non-unique, and alternative density configurations may produce comparably acceptable gravity responses. The final model is therefore treated as a regularized preferred density model consistent with the observed regional anomaly and adopted geological constraints, rather than as a unique reconstruction of the subsurface. Comparable regularized inversion approaches have been widely used to constrain density structure in other structurally complex settings (Constable et al., 1987; Oldenburg and Li, 2005; Tarhan Bal and Karcioglu, 2025). Compared with previous gravity studies in southern Java, which relied mainly on qualitative map interpretation, two-dimensional modelling, or more local three-dimensional models (Setiahadiwibowo et al., 2025), this study provides a regional-scale three-dimensional density-contrast model whose calculated response is consistent with the observed regional anomaly.

Gravity inversion produced a suite of density contrasts that fall within the expected range of lithological densities. Low-density domains are associated with non-consolidated alluvium and young volcanic units, whereas intermediate-density domains are characteristic of Miocene sedimentary and volcaniclastic successions, some of which include documented shale- and coal-bearing intervals associated with localized sediment accumulation within the evolving basin. Higher-density domains, in contrast, are associated with well-lithified carbonates, dense volcanic rocks, and intrusive bodies. This correlation provides additional evidence that the inversion is geologically reasonable and agrees with other studies that have used gravity to discriminate between lithologies at regional scales (Manger, 1963; Wang et al., 2012). Nevertheless, similar gravity responses may be produced by different combinations of lithology, porosity, alteration, weathering, and burial depth. For example, a relatively low-density anomaly may reflect sedimentary fill, strongly altered volcanic rocks, or highly porous volcaniclastics, whereas a high-density anomaly may result from crystalline volcanic rocks, intrusive bodies, or well-lithified carbonate units. The geological map and published stratigraphic information reduce the range of plausible interpretations,

but they do not eliminate this ambiguity. Accordingly, the density-to-lithology correlations used here represent the interpretations most consistent with the available geological framework.

The combined horizontal-derivative analysis and inversion cross-sections delineate several candidate structural boundaries characterized by lateral density contrasts. The strongest interpretations occur where prominent FHD gradients, SHD sign changes, and abrupt variations in the inversion density model coincide spatially. These features are interpreted as possible fault-controlled boundaries because their locations are consistent with the regional structural framework. However, derivative responses alone do not uniquely determine fault dip, displacement, or kinematics. The inferred normal and reverse fault styles should therefore be considered apparent structural interpretations supported by density-block relationships rather than direct determinations of fault geometry. Lower-amplitude derivative features, particularly those with weak FHD responses, are regarded as lower-confidence structural interpretations. In total, 15 candidate boundaries were identified (three along A-A′, three along B-B′, and nine along C-C′), of which five (A-A′ feature 1, B-B′ feature 3, and C-C′ features 7-9) are classified as lower-confidence. At the regional scale, the combined derivative and inversion results support a tectonically compartmentalized basin architecture rather than a laterally continuous sedimentary basin. Apparent normal-fault geometries and horst-graben to half-graben configurations are consistent with an earlier extensional stage that generated accommodation space and segmented depocenters. Although less confidently resolved, the apparent reverse structures are consistent with later compressional reactivation and tectonic inversion of inherited extensional faults, as documented elsewhere in Java and adjacent regions (Pulunggono and Martodjojo, 1994; Hall, 2012; Pham, 2024). This multiphase evolution plausibly explains the present-day juxtaposition of sedimentary, volcanic, carbonate, and intrusive density domains across the Southern Mountain Zone. The apparent horst-graben and half-graben geometries suggest that fault architecture may have influenced basin segmentation and sediment distribution.

The reconstructed structural framework also has broader implications for the regional petroleum system. Fault-controlled accommodation and basin compartmentalization may have influenced the accumulation, preservation, burial, and subsequent deformation of shale- and coal-bearing sedimentary intervals. Structural reactivation may likewise have modified the spatial relationships among potential source, reservoir, and sealing units and may have influenced fluid pathways. These implications, however, remain conceptual because the present gravity dataset does not directly constrain source-rock maturity, reservoir properties, sealing capacity, hydrocarbon migration, or trap integrity. Accordingly, petroleum-system significance is considered a regional geological implication of the reconstructed basin architecture rather than a direct exploration result of this study.

The principal limitation of this study arises from the inherent non-uniqueness of gravity inversion. The recovered density model depends on the adopted parameterization, initial density distribution, regularization strategy, model bounds, and regional-residual separation. In addition, the effective geological resolution of the GGMplus dataset should not be equated directly with its nominal grid spacing, particularly in rugged volcanic terrain where short-wavelength components (shorter than about 10 km) are derived largely from topography rather than observed gravity (Hirt et al., 2013); this is one reason why the analysis was restricted to wavelengths longer than 13.3 km. Therefore, small-scale density variations, individual fault throws, and detailed fault geometries remain uncertain. Independent constraints from seismic reflection, borehole data, magnetics, or other geophysical observations would be required to test and further refine the preferred density model. The present results should consequently be interpreted primarily at the regional scale, where they provide constraints on major density domains and candidate structural boundaries rather than a unique high-resolution geological reconstruction.

6. Conclusion

The Complete Bouguer Anomaly (CBA) ranges from −134.3 to 170.5 mGal across the study area, reflecting spatial variations in subsurface density contrasts. Because the CBA contains superimposed anomaly components of different wavelengths, regional-residual separation was applied before further interpretation. The resulting Regional Bouguer Anomaly ranges from −130.8 to 132.8 mGal and was obtained using RAPS-guided band-pass filtering, with the regional-residual boundary defined at approximately 0.05 cycles/km (20 km), a regional passband of 0.0125-0.05 cycles/km (80-20 km), and a transition band extending to 0.075 cycles/km (13.3 km). The filtered regional anomaly is interpreted as a regional-scale constraint on broad, longer-wavelength density variations rather than as a unique image of subsurface geological structure.

Sequential SVD-Occam inversion substantially improved the fit between the observed and calculated gravity responses. The normalized RMS data misfit decreased progressively from 15.5% to about 3.02%, indicating that each inversion stage contributed to a closer match with the measured gravity field. This improvement was achieved through a stepwise workflow that refined model-base geometry, density distribution, and block thickness. The combined SVD-Occam approach yielded a regularized preferred density model that provides an acceptable fit to the observed gravity data and remains consistent with the adopted geological constraints. However, the reduced RMS value reflects improved data fit only; it is neither a measure of geological accuracy nor an estimate of uncertainty in density, depth, or geometry, because the gravity inverse problem remains inherently non-unique.

Overall, the integrated regional gravity inversion and horizontal-derivative analysis indicates that the Southern Mountain Zone is characterized by a tectonically compartmentalized basin architecture rather than a laterally uniform subsurface. Broad density domains are separated by 15 candidate structural boundaries identified along the three inversion profiles, five of which are regarded as lower-confidence interpretations. These boundaries locally define apparent normal- and reverse-fault styles and horst-graben- to half-graben-like density-block geometries, although their dip, displacement, and kinematics are not uniquely resolved by the gravity data. The resulting structural configuration is consistent with a multiphase tectonic history involving extension and basin subsidence followed by structural reactivation and inversion. This fault architecture appears to have exerted an important control on the distribution of accommodation space, sedimentary depocenters, and the present juxtaposition of sedimentary, volcanic, carbonate, and intrusive domains. Shale- and coal-bearing successions documented within the region may therefore represent sedimentary records preserved within parts of this structurally segmented basin system. Their possible petroleum-system significance constitutes a broader regional geological implication, whereas the principal contribution of this study is the regional-scale characterization of basin architecture and tectonic compartmentalization.

Data availability statement. The data supporting this research comes from GGMplus (Global Gravity Model Plus), an open and publicly available dataset. The data can be accessed through the official website of Curtin University, Australia, at http://ddfe.curtin.edu.au/gravitymodels/GGMplus/

Acknowledgements. The authors wish to acknowledge the Education Scholarship, the Centre for Higher Education Funding, the Ministry of Higher Education, Science, and Technology of the Republic of Indonesia, and the Indonesia Endowment Fund for Education for providing financial support through a Doctoral Scholarship.

References

Alvandi, A., K. Su, H. Ai, V. E. Ardestani et al. (2023). Enhancement of Potential Field Source Boundaries Using the Hyperbolic Domain (Gudermannian Function), Minerals, 13, 10, doi:10.3390/min13101312.

Aster, R. C., B. Borchers and C. H. Thurber (2018). Parameter Estimation and Inverse Problems, 3rd ed., Academic Press, Cambridge, MA, 404, ISBN:978-0128046517.

Bachri, S. (2014). Pengaruh Tektonik Regional Terhadap Pola Struktur and Tektonik Pulau Jawa, JGSM, 15, 4, 215-221, doi:10.33332/jgsm.geologi.v15i4.60.

Blakely, R. J. (1995). Potential Theory in Gravity and Magnetic Applications, Cambridge University Press, Cambridge, 461, ISBN:978-0521415088.

Clements, B., R. Hall, H. R. Smyth and M. A. Cottam (2009). Thrusting of a volcanic arc: A new structural model for Java, Pet. Geosci., 15, 2, 159-174, doi:10.1144/1354-079309-831.

Constable, S. C., R. L. Parker and C. G. Constable (1987). Occam's inversion: a practical algorithm for generating smooth models from electromagnetic sounding data, Geophysics, 52, 3, 289-300, doi:10.1190/1.1442303.

Damayanti, C., S. Sismanto, A. Setiawan and L. Handayani (2025). Identifying the Basement Structure of the Sula Fault Zone in the Banggai-Sula Microcontinent Region, Molucca Sea, based on 2D Gravity Inversion Modelling using Particle Swarm Optimisation and 3D modelling using Grablox, Rud. Geol. Naft. Zb., 40, 2, 137-154, doi:10.17794/rgn.2025.2.10.

Kementerian Energi and Sumber Daya Mineral (ESDM) (2022). Peta Cekungan Sedimen Indonesia (Sedimentary Basin Map of Indonesia), Kementerian ESDM, Jakarta.

Farisan, A. and M. G. Rachman (2022). Carbonate rocks in northern of West Jiwo Hills Bayat: The indication of thrust belt development in southern Central Java, RISET Geol. Pertamb., 32, 2, 135, doi:10.14203/risetgeotam2022.v32.1218.

Gafoer, S. and N. Ratman (1999). Peta Geologi Lembar Jawa Bagian Timur (Geological Map of Eastern part of Jawa), Skala 1:500.000, Bandung: Pusat Penelitian dan Pengembangan Geologi.

Hall, R. (2012). Late Jurassic-Cenozoic reconstructions of the Indonesian region and the Indian Ocean, Tectonophysics, 570-571, 1-41, doi:10.1016/j.tecto.2012.04.021.

Hall, R., B. Clements, H. R. Smyth and M. A. Cottam (2007). A new interpretation of Java's structure, Proceedings of the Indonesian Petroleum Association, 31st Annual Convention and Exhibition, Indonesian Petroleum Association, Jakarta, 63-86.

Hassan, A. G. M., K. S. I. Farag, A. A. F. Aref and A. L. Piskarev (2024). Methods for 3D Inversion of Gravity Data in Indentifying Tectonic Factors Controlling Hydrocarbon Accumulations in the El Zeit Basin Area, Southwestern Gulf of Suez, Egypt, Geodyn. Tectonophys., 15, 2, 0751, doi:10.5800/GT-2024-15-2-0751.

Hinze, W. J., R. R. B. von Frese and A. H. Saad (2012). Gravity and Magnetic Exploration: Principles, Practices, and Applications, Cambridge University Press, Cambridge, 525, ISBN:978-0521871013.

Hirt, C., S. Claessens, T. Fecher, M. Kuhn et al. (2013). New ultrahigh-resolution picture of Earth's gravity field, Geophys. Res. Lett., 40, 16, 4279-4283, doi:10.1002/grl.50838.

Ismullah, M. F. M., M. Altin Massinai and Maria (2018). Shallow Depth Study Using Gravity and Magnetics Data in Central Java - Yogyakarta, J. Phys. Conf. Ser., 979, 1, 012046, doi:10.1088/1742-6596/979/1/012046.

Kafadar, Ö. (2019). Estimation of the Depth and Shape of the Source from Derivatives of Residual Gravity Data Using the Parametric Curves Technique: A Case Study from Erzincan-Çayırlı Region, Turkey, Erzincan Univ. Fen Bilimleri Enstitüsü Derg., 12, 1, 294-305, doi:10.18185/erzifbed.453364.

Kafadar, Ö. (2022). Applications of the Kuwahara and Gaussian filters on potential field data, J. Appl. Geophys., 198, 104583, doi:10.1016/j.jappgeo.2022.104583.

Kebede, H., A. Alemu and S. Fisseha (2020). Upward continuation and polynomial trend analysis as a gravity data decomposition, case study at Ziway-Shala basin, central Main Ethiopian rift, Heliyon, 6, 1, doi:10.1016/j.heliyon.2020.e03292.

Mammo, T. (2012). Analysis of gravity field to reconstruct the structure of Omo basin in SW Ethiopia and implications for hydrocarbon potential, Mar. Pet. Geol., 29, 1, 104-114, doi:10.1016/j.marpetgeo.2011.08.013.

Manger, G. E. (1963). Porosity and bulk density of sedimentary rocks, U.S. Geological Survey Bulletin 1144-E, U.S. Government Printing Office, Washington, DC, E1-E55, doi:10.3133/b1144E.

Menke, W. (2018). Geophysical Data Analysis: Discrete Inverse Theory, 4th ed., Academic Press/Elsevier, 350, ISBN:978-0128135563.

Nurhandoko, B. E. B., R. Kurniadi, S. Susilowati, K. Triyoso et al. (2019). Integrated Subsurface Temperature Modeling beneath Mt. Lawu and Mt. Muriah in the Northeast Java Basin, Indonesia, Open Geosci., 11, 1, 341-351, doi:10.1515/geo-2019-0027.

Oldenburg, D. W. and Y. Li (2005). Inversion for applied geophysics: A tutorial, Near-Surface Geophysics (D. K. Butler, ed.), Investigations in Geophysics, 13, Society of Exploration Geophysicists, Tulsa, doi:10.1190/1.9781560801719.ch5.

Ombati, D., J. Githiri, M. K'orowe and E. Nyakundi (2022). Delineation of Subsurface Structures Using Gravity Data of the Shallow Offshore, Lamu Basin, Kenya, Int. J. Geophys., 3024977, doi:10.1155/2022/3024977.

Oruc, B. and E. Balkan (2023). Mapping Crustal Structure and Deformation Using Gravity Data in the Bursa Basin and surroundings, Türkiye, Turk. J. Earth Sci., 32, 7, 931-943, doi:10.55730/1300-0985.1883.

Pham, L. T. (2024). Mapping the structural configuration of the northern part of the Central Indian Ridge from satellite gravity data using derivatives of the horizontal gradient, Adv. Space Res., 74, 4, 1648-1663, doi:10.1016/j.asr.2024.05.054.

Pirttijarvi, M. (2004). GRABLOX: Gravity interpretation and modelling software based on 3-D block model, user's guide, Report Q16.2/2004/2, Geological Survey of Finland, 1-31.

Pirttijärvi, M. (2014). GRABLOX: Gravity interpretation and modelling software based on a 3-D block model, Version1.6. Oulu: Department of Physics, University of Oulu, 1-58.

Prasetyadi, C., A. Subandrio, M. G. Rachman, A. R. F. Barizi et al. (2021b). Depositional Environment of Nampol Formation and Its Implications as Potential Source Rocks in the Sumbermanjing Area, South Malang, RSF Conf. Ser.: Eng. Technol., 1, 1, 78-94, doi:10.31098/cset.v1i1.374.

Prasetyadi, C., A. Subandrio, M. G. Rachman, A. R. F. Barizi et al. (2022). Source Rock Potential of Nampol Formation Sumbermanjing Area, Malang, East Java, Indonesia Based on Geochemistry Analysis of the Selected Sample, Sci. Contrib. Oil Gas, 45, 1, 53-63, doi:10.29017/scog.45.1.924.

Prasetyadi, C., A. Subandrio, M. G. Rachman, A. R. F. Barizi et al. (2021a). Subvolcanic Rock Petroleum System Potential in the South Malang Region, East Java, Indonesia, Open J. Yangtze Oil Gas, 06, 04, 146-160, doi:10.4236/ojogas.2021.64013.

Prasetyadi, C., I. Sudarno, V. Indranadi and Surono (2011). Pola dan Genesa Struktur Geologi Pegunungan Selatan, Provinsi Daerah Istimewa Yogyakarta dan Provinsi Jawa Tengah, Jurnal Geologi dan Sumberdaya Mineral (JSDG), 21, 2, hlm. 91-107, doi:10.1016/0743-9547(93)90003-8.

Prijosoesilo, P., Y. Sunarya and A. Wahab (1993). Recent progress of geological investigations in Indonesia, J. Southeast Asian Earth Sci., 8, 1-4, 5-23, doi:10.1016/0743-9547(93)90003-8.

Pulunggono, A. and S. Martodjojo (1994). Perubahan tektonik Paleogen-Neogen merupakan peristiwa tektonik terpenting di Jawa, Proceedings Geologi and Geotektonik Pulau Jawa, Yogyakarta, 37-50.

Rachman, M. G., S. Abhimantra, H. Ibadurrahman and K. Endarmoyo (2016). Preliminary study of hidrocarbon potential in intra-arc basin deposits: Case study on Jaten Formation, Dongko, Trenggalek, East Java, Indonesia, 9th AUN/SEED-Net Regional Conference on Geological and Geo-Resources Engineering, Bangkok, Thailand.

Rachman, M. G. and C. Prasetyadi (2021). Source Rock Potential of Nampol Formation in Sumbermanjing Area, Malang, East Java, Indonesia, Joint Convention Bandung 2021.

Safani, J., K. Ibrahim, W. A. Deni, A. L. Rubaiyn et al. (2023). Interpreting Structural Configuration of the Sengkang Basin of Indonesia Using Edge Detection and 3-D Euler Deconvolution to Satellite Gravity Data, Turk. J. Earth Sci., 32, 7, 894-914, doi:10.55730/1300-0985.1881.

Saibi, H., D. B. Hag, M. S. Mohammed Alamri and H. A. Ali (2021). Subsurface structure investigation of the United Arab Emirates using gravity data, Open Geosci., 13, 1, 262-271, doi:10.1515/geo-2020-0233.

Setiahadiwibowo, A. P., A. Setiawan, S. Husein and S. Sismanto (2025). Subsurface Structural Modelling using the Gravity Method in the Pacitan Area, Indonesia based on Derivative Analysis and Model Inversion, Rud. Geol. Naft. Zb., 40, 1, 51-61, doi:10.17794/rgn.2025.1.4.

Simav, M. and H. Yildiz (2021). Quantifying The Bathymetric Stripping Gravity Corrections of Global Seawater and Major Lakes over Turkey, Turk. J. Earth Sci., 30, 7, 916-927, doi:10.3906/yer-2105-38.

Smyth, H. (2005). East Java: Cenozoic basins, volcanoes and ancient basement, Proceedings of the Indonesian Petroleum Association, 30th Annual Convention and Exhibition, Indonesian Petroleum Association, Jakarta, 1, 251-266, doi:10.29118/ipa.629.05.g.045.

Soekarno, H., B. Pranoto, A. Restiana, A. A. Martha et al. (2025). Identifying Geological Fault Structures Using GGMplus Satellite Data and Derivative Methods to Characterize Mount Endut Geothermal Systems via 3D-Inversion Gravity Modeling, Geomatics Environ. Eng., 19, 3, 31-62, doi:10.7494/geom.2025.19.3.31.

Sribudiyani, N. Muchsin, R. Ryacudu, T. Kunto et al. (2003). The collision of the East Java microplate and its implication for hydrocarbon occurrences in the East Java Basin, Proceedings of the Indonesian Petroleum Association, 29th Annual Convention and Exhibition, Indonesian Petroleum Association, Jakarta, 1, 1-12, doi:10.29118/ipa.1530.03.g.085.

Sumintadireja, P., D. Dahrin and H. Grandis (2018). A note on the use of the second vertical derivative (SVD) of gravity data with reference to Indonesian cases, J. Eng. Technol. Sci., 50, 1, 127-139, doi:10.5614/j.eng.technol.sci.2018.50.1.9.

Sutasoma, M., A. Susilo, Sunaryo, E. A. Suryo et al. (2022). Analysis of the Rock Layer Contact Using the Gravity Data of Satellite Imagery and Resistivity Method, Int. J. GEOMATE, 23, 96, 69-76, doi:10.21660/2022.96.3306.

Tarhan Bal, O. and G. Karcioglu (2025). Three-Dimensional Inversion of Gravity Data Using the Levy PDF for Depth Weighting and a Rank Order Smoothing Constraint, Math. Geosci., 57, 3, 523-545, doi:10.1007/s11004-024-10173-2.

Telford, W. M., L. P. Geldart and R. E. Sheriff (1990). Applied Geophysics, 2nd ed., Cambridge University Press, Cambridge, 792, ISBN:9780521339384.

Vasanthi, A. and M. Santosh (2021). Overview of regional gravity field computation models and application of a novel method in imaging the lithospheric architecture and destruction of the North China Craton, Earth Sci. Rev., 215, 103548, doi:10.1016/j.earscirev.2021.103548.

Wang, G., Y. Zhu, S. Zhang, C. Yan et al. (2012). 3D geological modeling based on gravitational and magnetic data inversion in the Luanchuan ore region, Henan Province, China, J. Appl. Geophys., 80, 1-11, doi:10.1016/j.jappgeo.2012.01.006.

Wijayanti, D., R. T. Yulianto and M. I. Nurwidyanto (2009). Prediksi Batas Cekungan Jawa Timur Utara dengan Pegunungan Selatan di Daerah Magetan-Plaosan dengan Metode Gravitasi, JSM, J. Sains Mat., 17, 1, 54-61.

Witter, J. B., D. L. Siler, J. E. Faulds and N. H. Hinz (2016). 3D geophysical inversion modeling of gravity data to test the 3D geologic model of the Bradys geothermal area, Nevada, USA, Geotherm. Energy, 4, 14, doi:10.1186/s40517-016-0056-6.

Zhang, M. H., J. H. Qiao, G. X. Zhao and X. Y. Lan (2019). Regional gravity survey and application in oil and gas exploration in China, China Geol., 2, 3, 382-390, doi:10.31035/cg2018108.

***CORRESPONDING AUTHOR: Sismanto SISMANTO**,
Universitas Gadjah Mada, Faculty of Mathematics and Natural Sciences, Department of Physics,
Jl. Geografi, Yogyakarta, 55281, Indonesia
e-mail: sismanto@ugm.ac.id

© 2026 the Author(s).
Open Access. This article is licensed under a Creative Commons Attribution 4.0 International License